


Interband Tunneling in a Type-II Broken-Gap Superlattice

Andrzej Kolek *

Department of Electronics Fundamentals, Rzeszów University of Technology, al. Powstańców Warszawy 12, Rzeszów 35-959, Poland

 (Received 21 June 2022; revised 28 November 2022; accepted 1 February 2023; published 22 February 2023)

Due to its unique features, like tunable gap and high absorption coefficient, type-II superlattices receive growing interest. Substantial progress has been made in the technology of these materials as well as in the processing of superlattice-based devices. On the theoretical side, whereas the methods for superlattice analysis are well developed, for the superlattice-based devices they are well behind. Usually, such devices are modeled with semiclassical methods, in which the superlattice is treated as a bulk material having effective parameters extracted from its analysis with full quantum methods. As there is little theoretical justification for such a substitution, attempts have been made to model a whole superlattice-based device on a fully quantum level. In this paper, such modeling is presented for a broken-gap type-II superlattice diode: the nonequilibrium Green's function method is applied to the two-band model of an InAs/GaSb superlattice *p-i-n* diode. The focus is paid on the band-to-band (BTB) tunneling with the aim of an assessment of equations used for its semiclassical description. The results of calculations presented in the paper demonstrate that, in the superlattice diode, the BTB tunneling occurs only for certain values of the in-plane momentum k , for which electronic and hole subbands cross. This is in contrast to the bulk materials, for which there is a range of such k values. The simulations reveal much more differences. Accordingly, care must be taken when applying semiclassical models to describe the interband tunneling in superlattice devices.

DOI: [10.1103/PhysRevApplied.19.024059](https://doi.org/10.1103/PhysRevApplied.19.024059)

I. INTRODUCTION

Broken-gap type-II superlattices (T2SL) enable flexible engineering of the band gap in the range of energies covering mid- and long-wavelength infrared. Due to this feature, they attracted considerable attention as a very promising alternative for conventional mercury-cadmium-telluride (MCT) ternary [1]. Switching to this alternative material is, however, not straightforward because the bulk MCT material is replaced with a highly anisotropic stack of quasi-two-dimensional (2D) layers. The major difficulty concerns, in particular, the designing and optimization processes because different methods need to be used for the analyses. For MCT devices, the classical drift-diffusion (DD) model was commonly used to describe carrier transport. When applied directly to superlattice material, it would not account for the formation of minibands because, classically, any transport is forbidden in barrier layers.

Early attempts avoided this limitation by replacing T2SL with some virtual (bulk) material with a band gap and effective electron and hole masses derived either phenomenologically [2] or from quantum calculations [3–5].

This indirect method needs to be used with limited confidence as many quantum effects, including the miniband transport, are missed [6]. More advanced attempts incorporate an *effective quantum potential* instead of the real superlattice (SL) potential in the DD model [7] or a simplified single-band quantum model [8].

While catching a lot of underlying physics, these approaches are still unable to account for coherent interband components of the vertical current, which became important at high electric fields. For such purposes, the use of quantum methods applied to multi-band Hamiltonians is a must. Due to huge computational cost, an application of such methods to a macroscopic system is, in general, hardly possible. Therefore, hybrid classical-quantum approaches were proposed for such systems (see, e.g., Ref. [9] for a review). An example is the band-to-band (BTB) tunneling, which was included into the DD approach (similarly to other mechanisms) as the local generation rate

$$G_{\text{BTB}}(\mathbf{r}) = \pm \frac{1}{e} \nabla J_{\text{BTB}}(\mathbf{r}), \quad (1)$$

where J_{BTB} is the quantum BTB tunneling current carried by one type of carrier (either electrons or holes) [10–12].

*akoleknd@prz.edu.pl

In Ref. [12], the BTB current was calculated using nonequilibrium Green's function (NEGF) method. This method is quite general and can account not only for direct BTB tunneling but also for other processes, both coherent and incoherent. Due to this universality, in recent years, the NEGF method has been successfully used for studying quantum transport phenomena in various electronic devices. An incomplete list of its applications includes resonant-tunneling diodes [13], field effect [14] and tunneling [15] transistors, carbon nanotubes [16], light-emitting diodes [17–19], photodetectors [20–22], quantum well solar cells [23–25], quantum cascade [26–29], and interband [30] lasers and very recently also SL-based devices [31–34].

The vertical transport under high electric fields in T2SL broken-gap devices is almost completely unexplored within the quantum description. This paper tries to fill this gap; the NEGF method is used to study BTB tunneling in T2SL material, with the aim of (i) verifying the validity of simple semiclassical descriptions of this process, (ii) finding alternative approaches and descriptions that can replace this very complex and time-consuming method. Both these aims constitute rather qualitative than quantitative tasks, so the study is made with the simplest two-band model, which can account for interband tunneling.

II. MODEL

A. Two-band Hamiltonian

Although, comparing with Ref. [8], where single-band Hamiltonians were used, the use of a two-band model is a big step further; this model still seems to be a poor approximation because it entirely neglects the multivalley band structure of semiconductors. However, in the case of the materials used for the mid- and long-wavelength detection, it is worthwhile to state that this model is quite appropriate to detect general issues connected with the BTB tunneling because (i) in a direct band-gap InAs, which in these applications is commonly used for one of the SL layers, the Λ and Δ minima of the conduction band (CB) are far above the Γ minimum (about 0.72 and 1.0 eV, respectively) [35]; hence, they are not expected to provide a large contribution to the current. (ii) As for the valance band (VB), it was shown, by means of extensive atomistic and full-band quantum calculations, that for a direct band-gap material an approximation with a single dominant imaginary band connecting the VB and CB (inherent for a two-band model) agrees well with the more complicated models of the band structure (like, e.g., $sp^3d^5s^*$ tight binding) [15,36]. This observation justifies the use of two-band models for the description of the BTB tunneling in these types of materials. Consequently, the Wentzel-Kramers-Brillouin (WKB) approximation and Kane formula, which are based on a two-band Hamiltonian, were demonstrated

to work well for an InAs nanowire tunneling field-effect transistor [15]. More recent studies demonstrate an excellent agreement between the BTB currents obtained from full-band, atomistic quantum transport simulations and the calculations that use the two-band Flietner model solved both analytically [37] and by means of the NEGF method [38].

The device analyzed in this study uses InAs/GaSb SL. For such an SL, the sub-band alignment, necessary for the BTB tunneling, will be first attained between the first bound state of electrons in the Γ valley and the first quantized level of the heavy-hole (HH) band. Due to the anticrossing of light hole (LH) and HH dispersion branches, the imaginary dispersion is dominated by CB and LH components [39–41]. In the two-band Hamiltonian [see Eq. (2) below], the interaction between the bands (and so the dispersion) is described by the Kane parameter E_p , which is related to CB and VB bands' effective masses [39]

$$E_p = \frac{E_g}{2} [m_{\text{CB}}^{-1} + m_{\text{VB}}^{-1}].$$

For a suitable approximation of the interband tunneling in an InAs/GaSb SL, its value needs to be fitted with the LH effective mass, i.e., $m_{\text{VB}} = m_{\text{LH}}$. Obviously, this choice affects the real part of E - k_z dispersion and results in the decreased values of VB confinement energies (and so the miniband gaps).

It stems from the above considerations that the two-band model is more accurate at describing the imaginary than the real dispersions, and hence is quite suitable for approximating the interband tunneling in quantum confined devices (what is the scope of this paper) as opposed to the properties related to their energetic structure.

B. Device

The device is modeled with the 1D two-band $\mathbf{k} \cdot \mathbf{p}$ Hamiltonian [42]

$$H = \begin{bmatrix} E_c(z, k) & \hbar \sqrt{\frac{E_p}{2m_0}} \frac{d}{dz} \\ -\hbar \sqrt{\frac{E_p}{2m_0}} \frac{d}{dz} & E_v(z, k) \end{bmatrix}, \quad (2)$$

in which band energies are parametrized for the norm of the in-plane momentum $k_{||} \equiv k$ through kinetic energy terms, i.e., $E_{c,v}(z, k) = E_{c,v}(z) \pm \hbar^2 k^2 / 2m_{||e,h}$, where $m_{||e,h}$ are electron and hole in-plane effective masses, and z is the direction of transport. The typical band diagram of the device, which is an InAs/GaSb SL p - i - n photodiode terminated with bulk n -InAs and p -GaSb leads is shown in Fig. 1. The first hole (H1) and electron (C1) minibands are schematically depicted. It is clear that the dark current can be minimized if the doping is extended onto part of the SL region. In this case, the band bending makes both minibands face the forbidden gap in one of the terminations, so

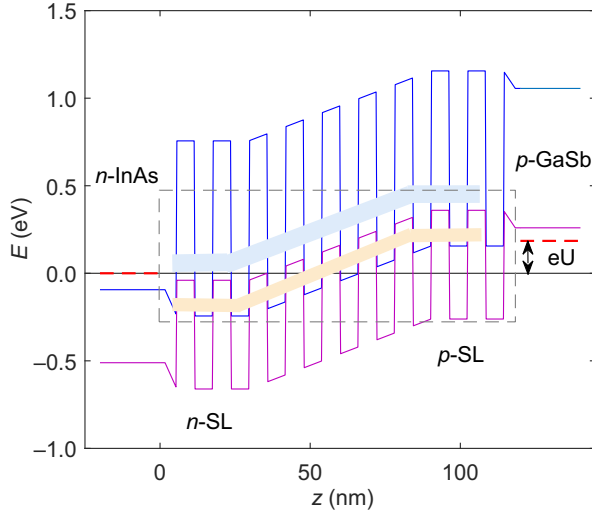


FIG. 1. Band diagram of the p - i - n InAs/GaSb SL device biased with voltage U . The first electron and hole minibands are schematically depicted. Dashed-line box outlines the window of calculations.

that the transport in the minibands is blocked: the contacts become carrier selective, which is required for the proper operation of the photovoltaic device [43].

C. Leads

Like other transport processes, the interband tunneling can be detected only when both leads extend to infinity. In the NEGF formalism, this extension can be mimicked by the so-called contact self-energies [44]. In the applied implementation, these self-energies are the single-value complex numbers, which add to the left and right-most diagonal element of a discretized Hamiltonian (see Appendix A).

D. Scatterings

The NEGF formalism enables the inclusion of scattering processes. Similarly to the leads, they can be taken into account through appropriate (scattering) self-energies. In the calculations, the scatterings with optical and acoustic phonons, and interface roughness (IR) are included. The formulations for respective self-energies are adapted from the seminal paper by Lake *et al.* [45]. In the implementation used in this paper, the scatterings with acoustic phonons and IR are local (diagonal) in real and energy spaces as opposed to scattering with longitudinal optical (LO) phonons, for which the fully nonlocal character in all spaces (z, k_{\parallel}, E) is preserved. This means that LO-phonon-assisted transitions, which originate in one band and finalize in the other band (phonon-assisted tunneling), are accounted for. Other interband processes, such as SRH, Auger, etc., are not accounted for.

III. NEGF METHOD

The equations of the NEGF formalism, discretized on the nonuniform real space grid, read [46]

$$\begin{aligned} (E\mathbf{I} - \mathbf{H} - \Sigma_{\text{lead}}^{\text{R}} - \Sigma_{\text{scatt}}^{\text{R}})\mathbf{G}^{\text{R}} &= \lambda \\ \mathbf{G}^{\text{<}} &= \mathbf{G}^{\text{R}}\lambda^{-1}(\Sigma_{\text{lead}}^{\text{<}} + \Sigma_{\text{scatt}}^{\text{<}})\mathbf{G}^{\text{R}\dagger} \\ \mathbf{G}^{\text{>}} &= \mathbf{G}^{\text{R}} - \mathbf{G}^{\text{R}\dagger} + \mathbf{G}^{\text{<}} \\ \Sigma_{\text{scatt}}^{\text{<}} &= \Sigma_{\text{scatt}}^{\text{<}}(\mathbf{G}^{\text{R}}, \mathbf{G}^{\text{<}}), \end{aligned} \quad (3)$$

where \dagger is the Hermitian operator, \mathbf{I} is the unity matrix, and Σ s and \mathbf{G} s are self-energy and Green's function (GF) matrices, which have the structure

$$\mathbf{G} = \begin{bmatrix} \mathbf{G}_{\text{cc}} & \mathbf{G}_{\text{cv}} \\ \mathbf{G}_{\text{vc}} & \mathbf{G}_{\text{vv}} \end{bmatrix}, \quad \Sigma = \begin{bmatrix} \Sigma_{\text{cc}} & \Sigma_{\text{cv}} \\ \Sigma_{\text{vc}} & \Sigma_{\text{vv}} \end{bmatrix}, \quad (4)$$

imposed by the structure of the Hamiltonian. The numbers defined in Eq. (A3) are the only nonzero elements of the Σ_{lead} matrix placed at first and last diagonal elements of the conduction band section Σ_{cc} . In contrast, Σ_{scatt} , which is the sum of $\Sigma_{\text{IR}} + \Sigma_{\text{phon}}$, is a full matrix (due to the nonlocal approximation of the LO-phonon scattering). The matrix λ is a diagonal matrix with the elements described by the local grid spacing, $\lambda_{ii} \equiv \lambda_i = 2/(z_{i+1} - z_{i-1})$.

It stems from Eqs. (2) and (3) that all \mathbf{G} s have the dimension of energy⁻¹length⁻¹ and are functions of two parameters, i.e., total energy E and in-plane momentum modulus k , $\mathbf{G} = \mathbf{G}(E, k)$. Then, densities of states (DOS), electrons (DOE), and holes (DOH), which are related to GFs, are the position-energy-momentum-resolved quantities. Specifically, the one-dimensional (1D) densities can be calculated from the diagonal elements of GF matrices summing over band contributions [23,47]

$$\begin{aligned} N(z_i, E, k) &= -\frac{1}{\pi} \text{Im}\{[\mathbf{G}_{\text{cc}}^{\text{R}} + \mathbf{G}_{\text{vv}}^{\text{R}}]_{ii}\} \text{ (DOS)}, \\ n(z_i, E, k) &= -\frac{i}{2\pi} [\mathbf{G}_{\text{cc}}^{\text{<}} + \mathbf{G}_{\text{vv}}^{\text{<}}]_{ii} \text{ (DOE)}, \\ p(z_i, E, k) &= -\frac{i}{2\pi} [\mathbf{G}_{\text{cc}}^{\text{>}} + \mathbf{G}_{\text{vv}}^{\text{>}}]_{ii} \text{ (DOH)}. \end{aligned} \quad (5)$$

The 1D quantities can be further integrated over \mathbf{k}_{\parallel} plane to get 3D densities. For the in-plane dispersion used in Eq. (2), it simplifies to merely multiplication of 1D densities by the factor $\Delta k^2/4\pi^2$, where Δk is the in-plane momentum grid spacing. The uniform sampling of k^2 space is used with $\Delta k^2 = 0.0044 \text{ nm}^{-2}$. The total energy is also uniformly sampled with the grid $\Delta E = 4 \text{ meV}$. Further details of the numerical model and parameters used in the simulations are provided in Table I.

The particle current can be calculated making use of a current operator whose diagonal elements are equal to the divergence of the current density [44, one should use the

TABLE I. Model and physical parameters.

	InAs	GaSb
Kane energy E_p (eV)	18.95	18.95
Band gap E_g (eV)	0.417	0.796
Layer width (nm)	6.06	6.06
Electron in-plane effective mass, $m_{ e}$ (eV)	0.022	0.042
Hole in-plane effective mass, $m_{ h}$ (eV)	0.022	0.042
Band offset $\Delta E_C, \Delta E_V$ (eV)	1.0, 0.621	
Number of SL periods	9	
Scattering time in the leads (ps) [26,28]	0.04	
Doping in left and right lead (cm^{-3})	$5 \times 10^{17}, 10^{18}$	
Temperature (K)	300	
LO-phonon energy, E_{LO} (meV)	30	
Screening length, λ_{Debye} (nm)	7.68	
Dielectric constant, $\epsilon_0/\epsilon_\infty$	15.15/12.3	
IR correlation function, length, height (nm)	Gaussian/9/0.15	
Deformation potential (eV)	5.89	
Density (kg/m^3)	5680	
Sound velocity (m/s)	4810	
Maximum grid spacing, Δz_{max} (nm) [48]	1.817	
Energy grid, ΔE (meV)	4	
Momentum squared grid, Δk^2 (nm^2)	0.0044	

GFs integrated over grid spacing, $\mathbf{G}^<\lambda^{-1}$, in Eq. (8.6.3) therein], [12]

$$\nabla J(z_i, E, k) = \lambda_i \text{Tr}[\mathbf{H}\mathbf{G}^<\lambda^{-1} - \mathbf{G}^<\lambda^{-1}\mathbf{H}]_{ii},$$

where trace is over band indices (\mathbf{c}, \mathbf{v}). The z -resolved spectral current density $J(z_i, E)$ can be calculated by integrating the divergence ∇J over z and k

$$J(z, E) = \frac{e}{\pi \hbar} \int \frac{dk^2}{8\pi^3} \int_0^z dz' \nabla J(z', E, k).$$

The total current can be obtained integrating $J(z, E)$ over E in the entire range of energies (must conserve to validate the consistency of the solution). The interband current can be obtained by limiting the integration to one of the bands

$$J_{n,p}(z) = \int_{E \subset \text{one band}} J(z, E) dE. \quad (6)$$

One can use these currents, e.g., in Eq. (1), to estimate quantum insert to DD equations (see Appendix B).

IV. RESULTS

A. Interband tunneling

Under operating conditions, photovoltaic devices work with reverse bias. The diagram shown in Fig. 1 corresponds to this case. For sufficiently high bias voltages, C1 and H1 minibands cross, and so the interband tunneling current, either direct (Zener) or phonon assisted, may flow.

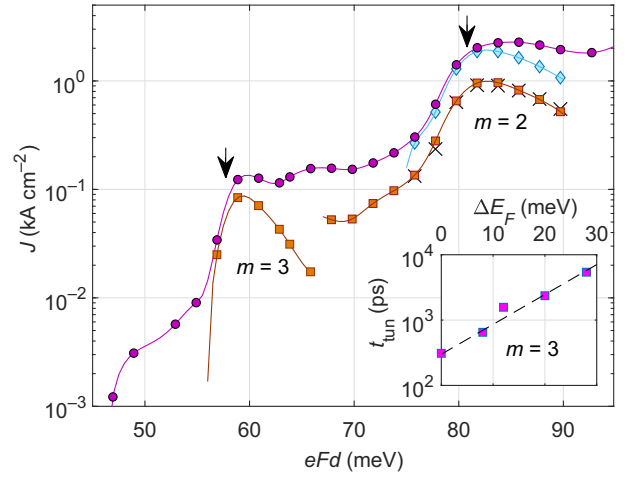


FIG. 2. Current-voltage characteristics calculated for the reversed bias T2SL diode shown in Fig. 1. Arrows indicate the position of the resonances calculated with Eq. (8) for $m = 2$ and $m = 3$. Data series correspond to the following: circles, total current; squares and crosses, single BTB transition between Wannier-Stark states; diamond, the sum of two BTB transitions for $m = 2$. Inset: tunneling times for $m = 3$ versus the difference between Wannier-Stark energies at $k = 0$.

In bulk homojunction devices, the Zener current has an exponential current-field dependence [49,50]

$$J_{\text{BTB}}(z) \sim \exp\left(-\frac{\pi \sqrt{m_r} E_g^{3/2}}{2eF\hbar}\right). \quad (7)$$

In SL material at sufficiently high electric field F , the minibands break into Wannier-Stark (WS) states. They act as resonant centers for the BTB tunneling process; each time when the WS state in the conduction band becomes energetically aligned with the WS state in the valence band, the tunneling current is enhanced. This makes the current-voltage (I - V) characteristic have an oscillatory structure. Such oscillations are observed in devices made of high-quality materials, in which a defect-assisted tunneling did not hide the direct tunneling current [51–55]. The simulations presented in Figs. 2–4 in general confirm this scenario.

The oscillatory structure of the I - V curve is well reproduced in Fig. 2. Current maxima coincide well with the resonance condition

$$eF \left(m + \frac{1}{2}\right) d = \Delta E_g, \quad (8)$$

where d is the SL period, ΔE_g is the C1-H1 band gap, and $m + \frac{1}{2}$ is the number of SL periods spanned by the tunneling process. Equation (8) is valid for the homogeneous electric field, which can be found well in the

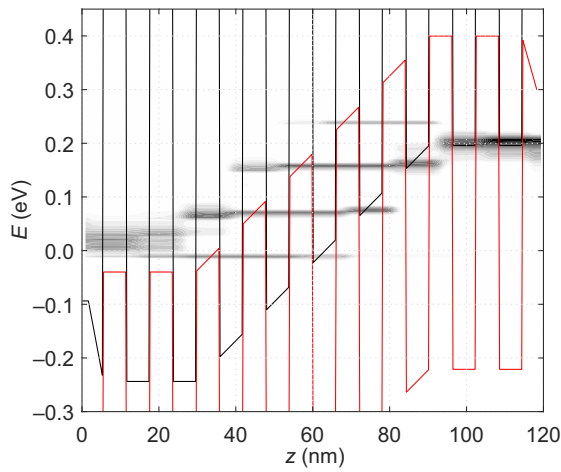


FIG. 3. Position-resolved spectrum of current flowing in the structure. Stripes in the graph center correspond to the tunneling between Wannier-Stark states. The most upper and lower stripe corresponds to the tunneling between the Wannier-Stark state and the miniband in the p - and n -doped contacts. Band diagram of the simulated device is also shown for the bias $U = -195$ mV.

depletion layer. Spatially resolved current spectrum presented in Fig. 3 reveals that the transitions indeed occur in this region. They occur in addition to the transition that takes place at the border of the depletion layer between H1 miniband and WS states in the conduction band. In the literature, only the latter were postulated to interpret current oscillations [51,53,56]. The other difference is that WS states were postulated to create only a resonance that mediates the transitions, which finally reach continuum states of the n region [51]. The data presented in Fig. 3 reveal that *WS states are the final states of the BTB transitions*,

from which the carriers are transported towards the lead by intraband hopping between WS states formed out of the minibands [6].

Limiting the integration to a certain energy window, one can study the individual BTB transitions. Data series labeled $m = 2$ and $m = 3$ in Fig. 2 correspond to the transitions between WS states, which are separated by $m + \frac{1}{2}$ lattice periods. They are observed in different ranges of the electric field. The z -resolved current spectrum in Fig. 3 is calculated for the field approximately equal to 67.5 kV/cm, which maximizes the current for $m = 2$. The value of m can be identified directly not only from the energy-resolved local DOS but also from the current spectrum in Fig. 3, as the length of the *thin* part of the stripes. Their brush-like endings occur due to carrier transport within the WS sub-bands caused by inelastic scatterings. The maxima of individual BTB transitions occur when the WS states in the conduction and valence bands align for the vanishing in-plane momentum. In this case, the barriers for the tunneling process are the lowest.

Due to the opposite curvatures of E - k dispersion of the hole and electron subbands, the alignment of the WS states can also occur for nonzero k values. In this case, the barriers for the tunneling process increase by the sum of the in-plane energies $\hbar^2 k^2 / 2m_{||h} + \hbar^2 k^2 / 2m_{||e}$, which makes the transmission coefficient exponentially decrease with k increasing. Consequently, the current at higher k 's is damped exponentially. This scenario applies, however, only to the fields larger than the field that maximizes the interband current (make WS states align for $k = 0$), as only in this case WS sub-bands may cross. For lower fields (voltages), sub-bands do not cross, so direct BTB transition is impossible. The phonon-assisted tunneling is still possible, provided the gap between the WS subbands is less

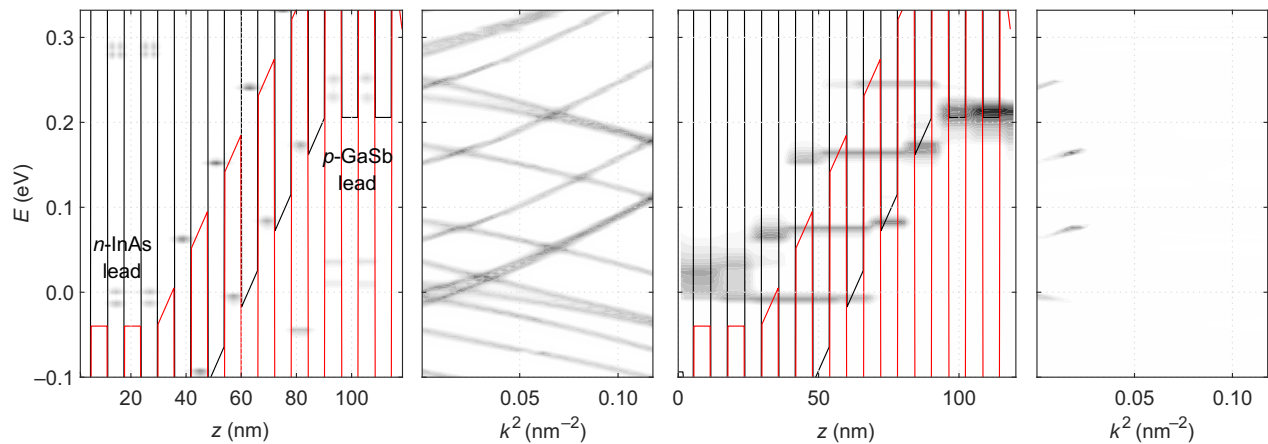


FIG. 4. (a) Band diagram for the reverse-biased device ($U = -0.235$ V) and DOS for vanishing in-plane momentum $k = 0$. In the central part, minibands are broken into Wannier-Stark states. (b) Spatially averaged DOS as the function of k^2 ; dark lines show hole and electron sub-bands formed by the Wannier-Stark states. (c) Position-resolved spectrum of the flowing current. (d) Momentum-energy-resolved current density in the center of the device, $J(E, k, z = 63$ nm); current flows at k 's, for which electron and hole WS sub-bands cross.

than LO-phonon energy. All these issues are illustrated in Fig. 4.

One more conclusion that can be derived from Fig. 2 is that individual BTB currents additively contribute to the total current: in the range of fields ($76 < eFd/\text{meV} < 82$), where only two ‘ $m = 2$ ’ transitions contribute to the total current, their sum fits exactly the value of the total current. In a real device with hundreds of SL periods, the BTB tunneling current can then be estimated as

$$J_{\text{BTB}} = N_{\text{SS}} \sum_m J_{\text{SS}}(m), \quad (9)$$

where N_{SS} is the number of periods in the “ i ” section of the p - i - n diode from which the WS transitions may originate (one can estimate N_{SS} as the total number of the lattice periods N minus those excluded by the carrier-selective contacts, $N_{\text{SS}} = N - 2\Delta E_g/eFd$), and $J_{\text{SS}}(m)$ is the current of individual interband WS-to-WS transition that spans $m + \frac{1}{2}$ lattice periods. The simulations show that the transitions for $m = 2$ and $m = 3$ matter. The one for $m = 1$ would occur for very strong electric fields, which would lead to material breakdown, the issue not discussed in this paper. For lower fields, the transitions for larger m prevail. They decay exponentially with m increasing (decreasing field), but should be taken into account unless they are hidden by inelastic and/or trap-assisted btb processes.

B. In-band transport

The I-V characteristic connected with the single WS-to-WS transition is described not only by the process of interband tunneling but also by the in-band parts of the current path. In the range of fields depicted in Fig. 2, the in-band transport is dominated by the WS hopping [6]. Its contribution to the I-V characteristic can be estimated comparing the currents obtained for devices with different numbers of SL periods. The simulations performed for the device shorter by one SL period give the maximum current of the single transition through 2.5 periods ($m = 2$) larger by $\approx 30\%$. Such an increase is unexpected for bulk devices and results from the fundamental difference of the interband tunneling in bulk and SL materials, which is illustrated in Fig. 5.

In both cases, the process takes place well in the depletion region, and each tunneling event generates an electron in the conduction band and a hole in the valence band. In the bulk material, the states occupied by these newly generated carriers are in good contact with the leads, so they are almost immediately removed to cathode/anode in a fast coherent (ballistic) process, so that the tunneling transition is the main bottleneck. In the SL material, the electron and hole are transported toward the leads within minibands by an inelastic scattering process. The velocity of this process is field-dependent and limited by the miniband width W

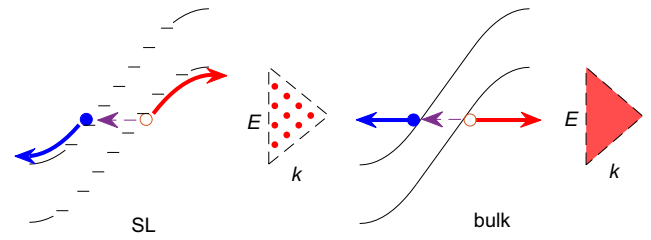


FIG. 5. Schematic illustration of btb tunneling in SL and bulk materials. Arrows illustrate the single btb transition and the extraction path of the created e - h pair. The number of transitions is depicted in E - k space.

and elastic and inelastic scattering times [6]

$$v_{\text{drift}} < \sqrt{\frac{\tau_{\text{in}}}{\tau_{\text{in}} + \tau_{\text{el}}}} \frac{v_m}{2}, \quad v_m = \frac{d|W|}{\hbar}, \quad (10)$$

which for the present case gives the maximum value of 3.4×10^6 cm/s. This value is reached for the field

$$F_{\text{max}} \approx \frac{\hbar}{ed\tau}, \quad (11)$$

determined by the effective scattering time, $\tau \equiv (\tau_{\text{in}}\tau_{\text{el}})^{\frac{1}{2}}$. In InAs/GaSb SL, used for the infrared detection, the value edF_{max} usually does not exceed 10 meV. According to Eq. (8), for such a field, interband transitions are unlikely, as they would have spanned too many ($m \gg 1$) SL periods. At higher electric fields, for which the distance is “tunnelable,” the drift velocity is reduced approximately in the $1/F$ manner. In this range, the minibands split into a Wannier-Stark ladder, so that the in-band transport relies on hopping between WS states. Simulations reveal that when the field increases to approximately equal to 70 mV/period, for which the interband transitions have been observed (see Fig. 2), the velocity drops to approximately equal to 1.5×10^6 cm/s (see Fig. 6).

In order to get this estimate, one needs to “unblock” the possibility for free drift of the carriers within the miniband. The way to realize this condition could be, e.g., leaving the entire SL region undoped and terminating the SL with the same type of the leads. Results of such simulations are shown in Fig. 6. In general, they fit well to the two-time model of miniband transport [57]

$$v_{\text{drift}} = v_m \frac{edF\hbar/\tau_{\text{in}}}{(\hbar/\tau)^2 + (edF)^2}, \quad (12)$$

in which the inelastic scattering time τ_{in} is field dependent and is reduced by some amount each time when the WS states, localized in the periods spaced by distance md , are separated by the energy $eFdm = E_{\text{LO}}$. In this case, the fast emission and/or absorption of the LO phonon is possible, which produces resonances in the I - V curve [58–60].

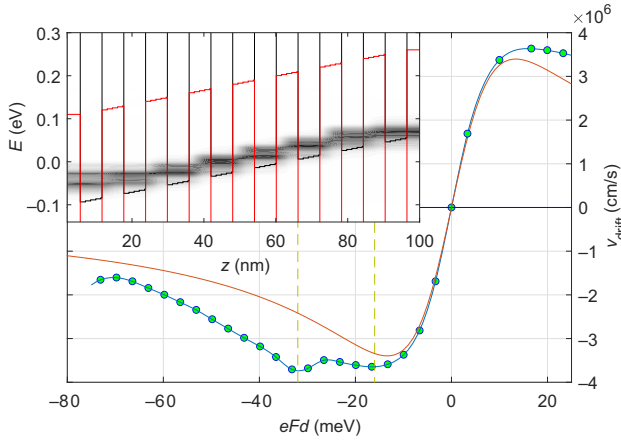


FIG. 6. Drift velocity in the H1 miniband of the 20/20 ML InAs/GaSb SL terminated on both sides with GaSb leads. Red line is the plot of Eq. (12). Vertical dashed lines are localized on the horizontal axis at $eFd = E_{LO}$ and $2eFd = E_{LO}$. Inset: energy-position-resolved current density in the structure biased by $U = 0.15$ V ($eFd = 16.5$ meV).

V. APPLICATION TO PHOTOVOLTAIC DEVICE

Having the value of the drift velocity determined, one can estimate the transit time through the device. For a device with $100 \times (20 \text{ ML}/20 \text{ ML})$ SL absorber, the transit time takes approximately $t_{\text{tran}} = 80$ ps. This value needs to be compared with the tunneling time of the BTB tunneling transition. It can be estimated as the ratio of the sheet electron density n_{sheet} at the origin (i.e., the WS in the valence band) to the interband current density. The former is determined by the energetic width ΔE of the single stripe in the interband current spectrum, which, on the other hand, is determined by the broadening of WS states

$$n_{\text{sheet}} = n_{2D} \Delta E. \quad (13)$$

Plots like these in Fig. 3 allow estimation of the $\Delta E = 8$ meV for both $m = 2$ and $m = 3$ transitions. Using $n_{2D} = m_{||h}/\pi \hbar^2$, one obtains the theoretical estimate $n_{\text{sheet}} \approx 1.4 \times 10^{11} \text{ cm}^{-2}$. The NEGF estimate can be obtained by integrating 1D DOE, available as the output from the simulations [see Eq. (5)], over in-plane momentum, energy, and real space. Numerical estimates are $1.27 \times 10^{11} \text{ cm}^{-2}$ for $m = 2$ and $1.53 \times 10^{11} \text{ cm}^{-2}$ for $m = 3$. They are not far from the theoretical value. The corresponding tunneling times are $t_{\text{tun}} \approx 25$ ps for $m = 2$, and $t_{\text{tun}} \approx 300$ ps for $m = 3$ transitions.

The comparison of tunneling and transit times allows for the conclusion that in the case of tunneling through few numbers of lattice periods ($m \leq 2$), the BTB transition introduces the impedance much lower than the one introduced by the in-band transport. The BTB tunneling current is described by the velocity given by Eq. (12) and the

number of tunneling spots (approximately equal to lattice periods). However, this is the range of high fields, which is unlikely under the operating conditions of the photovoltaic absorber (except for the near-contact regions [2]).

At low fields, the tunneling times are much longer than the in-band transit time and dominate the transport. The BTB current is then described by Eq. (9), in which summation over m is restricted to lowest m , which ensures the crossing of the sub-bands, i.e.,

$$m_F = \text{ceil}(\Delta E_g/eFd), \quad (14)$$

where $\text{ceil}(x)$ is the nearest integer greater than x . The difference $\Delta E_F \equiv m_F eFd - \Delta E_g$ is the amount of energy by which the WS states in C1 and H1 mismatch each other at $k = 0$. An increase of the in-plane momentum cancels this mismatch but simultaneously results in the increase of the barrier height, and so the tunneling time. The dependence

$$t_{\text{tun}}(m, \Delta E_F) = t_{\text{tun}}(m, 0) e^{\Delta E_F/\alpha_m} \quad (15)$$

is expected, where the parameter α_m describes the dumping of the tunneling transition due to the in-plane movement and can be estimated from t_{tun} vs. ΔE_F plots; the value $\alpha_3 = 10$ meV is found using the data depicted in Fig. 2 (see the inset).

In a p - i - n photodiode, the absorber is usually undoped and possesses a weak and uniform electric field. Under such operating conditions, the BTB tunneling current can be approximated as

$$J_{\text{BTB}} = (N - \Delta E_g/eFd) \frac{em_{||h} \Delta E}{\pi \hbar^2 t_{\text{tun}}(m_F, \Delta E_F)}, \quad (16)$$

where all parameters have been already defined. Two of them, i.e., current broadening ΔE and tunneling time that obey Eq. (16), need to be estimated with the use of quantum methods. The procedure of their estimation is proposed in this section.

VI. SUMMARY AND CONCLUSIONS

Theoretical issues related to electrical transport in T2SL devices in many aspects need to be solved with the use of quantum methods. One of them is the interband tunneling because, in general, the DD approach cannot account for this quantum phenomenon. The analysis made by means of NEGF method reveals that the interband tunneling in T2SL devices is very different from that in bulk devices. The difference concerns mainly the energy domain. In the bulk device, the entire event, which includes tunneling transition and extraction of carriers from the depletion region, runs at fixed energy in a scattering-free process. In the SL

device, the energy is conserved only for tunneling. Carrier extraction proceeds in a dissipative and scattering-rich process.

Another difference concerns the number of states available for the tunneling event. Their population is described by the overlap of the densities of states (DOS) on both sides of the tunneling transition. In bulk devices, there are plenty of such states resulting from the overlap of (continuous in E) 1D densities. In the SL material, there are few of them because the DOS in this material is a comb of Lorentzians centered at the energies of WS states (see Fig. 5).

Due to the above differences, the WKB result of Eq. (7), often employed to estimate the BTB tunneling current in the bulk junction, cannot be used for SL devices. Instead, for medium electric fields, the BTB current can be approximated by Eq. (16) with some of the parameters evaluated with quantum methods. At high field, the BTB tunneling is not a bottleneck. It is rather the in-band hopping between the WS states, and appropriate transport models can be employed in this region to estimate the current (NEGF is one of them). At low fields, BTB tunneling is unlikely, similarly to bulk devices, because of the tunneling distance increased to very long values.

All the above issues have been detected with the simple two-band model, which, however, as stated in the end of Sec. II A, is able to catch well the basic physics of the BTB tunneling. To get a more quantitative picture of real devices, more elaborated Hamiltonians are necessary. Attempts to employ multiband $\mathbf{k} \cdot \mathbf{p}$ Hamiltonians to model T2SL with the NEGF method are now in progress [21,32,59]; so far, only in Ref. [32], the BTB current was observed but not systematically studied.

As for other types of devices, some analogy can be found in the so-called electron-hole bilayer tunneling field-effect transistors (EHBTFET), in which, like in the SL, the tunneling occurs between 2D gases, which both are quantum confined in the direction of transport (2D-2D face tunneling) [40,61]. Quantum models for such devices were elaborated [61] but not with the NEGF method. It is in contrast to nanowire tunneling field-effect transistors, for which a large amount of NEGF-based studies exists. In these devices, however, the quantum confinement occurs perpendicular to the transport direction (edge tunneling), which makes the physics of BTB tunneling process quite different.

Due to the lack of more elaborated NEGF studies devoted to 2D-2D face tunneling, the results presented in this paper need to be referred to analytical results obtained for direct band-gap EHBTFETs, in which the direct BTB current dominates: in general, in analogy to Fig. 2, they confirm the oscillatory structure of I - V characteristic with the bumps, which occur when the electron and hole sub-bands align [40,61].

ACKNOWLEDGMENTS

This research is supported by the National Science Centre, Poland, under Project No. UMO-2020/37/B/ST7/01830 (OPUS-19).

APPENDIX A: DERIVATION OF CONTACT SELF-ENERGY

In the applied implementation of the NEGF method, the 1D Hamiltonian of Eq. (2) is discretized in real space using a one-sided right and left derivative for the conduction and valence component

$$\frac{d\varphi_i^c}{dz} = \frac{\varphi_{i+1}^c - \varphi_i^c}{\Delta z_{i,i+1}}, \quad \frac{d\varphi_i^v}{dz} = \frac{\varphi_i^v - \varphi_{i-1}^v}{\Delta z_{i-1,i}}.$$

Such a discretization results in the form of \mathbf{H} matrix identical to the two-band tight-binding Hamiltonian [23], and benefits from the single-element form of the matrix

$$\boldsymbol{\tau} = V \begin{bmatrix} 0 & 0 \\ -1 & 0 \end{bmatrix}, \quad V = \frac{\hbar}{\Delta z_{i,i+1}} \sqrt{\frac{E_p}{2m_0}},$$

which couples subsequent layers ($i, i+1$) of a discretized system. The usual approach for the calculations of electronic transport with the NEGF method is to cut \mathbf{H} at device boundaries, keeping the interaction with the leads through contact selfenergies [44]. Assuming that sites 0 and 1 are the rightmost and leftmost sites in the lead and device, the self-energy of the left contact (for the device) can be calculated as [44]

$$\boldsymbol{\Sigma}_{\text{lead}}^{\mathbf{R}} = \boldsymbol{\tau}' \mathbf{g}^{\mathbf{R}} \boldsymbol{\tau} = \boldsymbol{\Sigma}_{\text{lead}}^{\mathbf{R}} = V^2 \begin{bmatrix} g_{00v}^{\mathbf{R}} & 0 \\ 0 & 0 \end{bmatrix}, \quad (\text{A1})$$

where $\mathbf{g}^{\mathbf{R}}$ is the surface Green's function (GF) of the uncoupled semi-infinite lead, and $g_{00v}^{\mathbf{R}}$ is the valence part of its rightmost element, i.e., $g_{00v}^{\mathbf{R}} \equiv [\mathbf{g}_{00}^{\mathbf{R}}]_{2,2}$. It stems from Eq. (A1) that the only nonzero element of the left-contact self-energy matrix appears at the position of the conduction-band component of the leftmost layer, $i=1$.

The surface GF needed to calculate its value can be calculated in the Gedanken experiment relying on expanding the semi-infinite lead by one more layer. The Dyson equation for a one-layer device left connected to the semi-infinite lead takes the form

$$\begin{bmatrix} E - E_c - V^2 g_{00v}^{\mathbf{R}} & -V \\ -V & E - E_v \end{bmatrix} \begin{bmatrix} g_{00c}^{\mathbf{R}} & g_{00cv}^{\mathbf{R}} \\ g_{00vc}^{\mathbf{R}} & g_{00v}^{\mathbf{R}} \end{bmatrix} = \begin{bmatrix} 1 & 0 \\ 0 & 1 \end{bmatrix}, \quad (\text{A2})$$

which utilizes the obvious conjecture that elements of the matrix $\mathbf{g}^{\mathbf{R}}$ for original and extended lead should be identical. Solving Eq. (A2) for $g_{00v}^{\mathbf{R}}$ and using Eq. (A1), one gets

[62]

$$\Sigma_{\text{lead}}^R = V^2 g_{00v}^R = \frac{E - E_c}{2} \pm V \sqrt{\left(\frac{E - E_c}{2V}\right)^2 - \frac{E - E_c}{E - E_v}}, \quad (\text{A3})$$

where $E_{c,v}$ are the band edge energies in the lead (for a given k). The lesser contact self-energy can be calculated as $\Sigma_{\text{lead}}^< = \Sigma_{\text{lead}}^R f_{\text{lead}}$, where f_{lead} is the Fermi function in the lead [44,45].

APPENDIX B: MULTISCALE MODELING OF SL DEVICE

In the DD models, the interband processes describing the creation and annihilation of electron-hole pairs are included through generation and recombination rates in the semiconductor transport equations. As a rule, the SRH, Auger, and radiative recombination rates are included in the simulations (e.g., via the ABC model [63]). The BTB tunneling process also creates an e - h pair, and the common way of its inclusion is to add the BTB generation rate G_{BTB} to the continuity equation [10–12]. Hurkx *et al.* [10] proposed to localize this rate in the center of the gap (at the energy of the transition). This idea has been adapted in the very recent work by Tibaldi *et al.* [12].

In terms of the nomenclature used in Ref. [64], the NEGF calculations can be *coupled* or *linked* (depending on computational resources and how detailed the simulations are) to DD simulations within the *overlapped* scheme where the *microscopic* (NEGF) model provides a generation rate to the *macroscopic* (DD) model. The possibility for *concurrent multiscale simulation* (coupling both models) is also possible as the BTB generation rate can be calculated for potential profile and quasi-Fermi-levels passed to the NEGF solver from the DD simulator. The latter may utilize the two-band model with effective masses and band gap equivalent to the C1-H1 minibands.

Depending on how detailed the DD simulation is, the BTB generation rate can be sent to the DD solver as a quantity, either resolved in various domains (position, energy, transverse momentum), or integrated over some of them. The simplest example of the latter is the rate calculated as the ratio of the BTB current density and a tunneling distance [11]: $G_{\text{BTB}} = J_{\text{BTB}}/el_{\text{tun}}$, where $l_{\text{tun}} = \Delta E_g/eF$. Using the data from Fig. 2, one gets, e.g., $G_{\text{BTB}} = 2.25 \times 10^{27} \text{ cm}^{-3} \text{ s}^{-1}$ /per transition for the field $F = 67.5 \text{ kV/cm}$.

An example of the former is presented in Fig. 7. The z -resolved spectral generation rate is calculated following the idea of Refs. [10,12] defining a delimiter line, which separates electron and hole contributions to the spectral current in the center of the C1-H1 minigap (see Fig. 7). This line defines the limits of the integration in Eq. (6). One can also localize the calculated tunneling rate at the

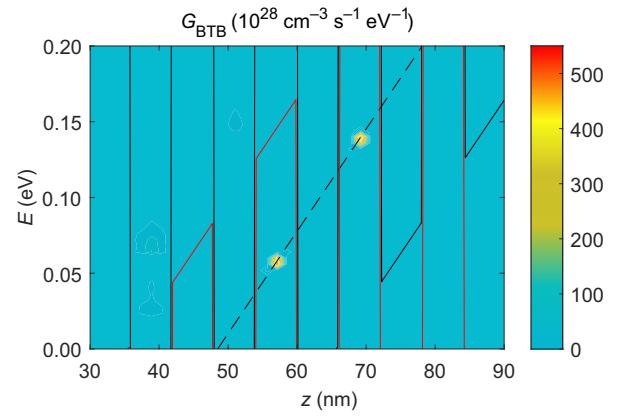


FIG. 7. Energy-position-resolved BTB tunneling rate, G_{BTB} , in the central part of the SL absorber (under the field $F = 67.5 \text{ kV/cm}$) for the vanishing in-plane momentum, $k = 0$ (color map). SL band edges and delimiter line (dashed) are also shown.

position of band edges (at energy E) to get the nonlocal approximation of this process. Another possibility of coupling the NEGF and DD models would use the analysis presented in Sec. V; the NEGF solver passes to the DD master all parameters of Eq. (16), enabling thus its use in the calculations of the BTB generation rate.

- [1] A. Rogalski, P. Martyniuk, and M. Kopytko, InAs/GaSb type-II superlattice infrared detectors: Future prospect, *Appl. Phys. Rev.* **4**, 031304 (2017).
- [2] M. Delmas, J.-B. Rodriguez, and P. Christol, Electrical modeling of InAs/GaSb superlattice mid-wavelength infrared pin photodiode to analyze experimental dark current characteristics, *J. Appl. Phys.* **116**, 113101 (2014).
- [3] F. Fuchs, E. Ahlswede, U. Weimar, W. Pletschen, J. Schmitz, M. Hartung, B. Jager, and F. Szmulowicz, Magneto-optics of InAs/Ga_{1-x}In_xSb infrared superlattice diodes, *Appl. Phys. Lett.* **73**, 3760 (1998).
- [4] P. Martyniuk, J. Wrobel, E. Plis, P. Madejczyk, W. Gawron, A. Kowalewski, S. Krishna, and A. Rogalski, Modeling of midwavelength infrared InAs/GaSb type II superlattice detectors, *Opt. Eng.* **52**, 061307 (2013).
- [5] F. Szmulowicz, H. J. Haugan, and G. J. Brown, Analysis of (110) indium arsenide–gallium antimonide superlattices for infrared detection, *J. Appl. Phys.* **104**, 074505 (2008).
- [6] A. Wacker, Semiconductor superlattices: A model system for nonlinear transport, *Phys. Rep.* **357**, 1 (2002).
- [7] T.-Y. Tsai, K. Michalczewski, P. Martyniuk, C.-H. Wu, and Y.-R. Wu, Application of localization landscape theory and the $k \cdot p$ model for direct modeling of carrier transport in a type II superlattice InAs/InAsSb photoconductor system, *J. Appl. Phys.* **127**, 033104 (2020).
- [8] A. Tibaldi, J. A. Gonzalez Montoya, M. Vallone, M. Goano, E. Bellotti, and F. Bertazzi, Modeling Infrared Superlattice Photodetectors: From Nonequilibrium Green's Functions to Quantum-Corrected Drift Diffusion, *Phys. Rev. Appl.* **16**, 044024 (2021).

- [9] M. Auf der Maur, Multiscale approaches for the simulation of InGaN/GaN LEDs, *J. Comput. Electron.* **14**, 398 (2015).
- [10] G. Hurkx, D. Klaassen, and M. Knuvers, A new recombination model for device simulation including tunneling, *IEEE Trans. Electron Devices* **39**, 331 (1992).
- [11] A. Schenk, Rigorous theory and simplified model of the band-to-band tunneling in silicon, *Solid State Electron.* **36**, 19 (1993).
- [12] A. Tibaldi, J. A. G. Montoya, M. G. C. Alasio, A. Gullino, A. Larsson, P. Debernardi, M. Goano, M. Vallone, G. Ghione, E. Bellotti, and F. Bertazzi, Analysis of Carrier Transport in Tunnel-Junction Vertical-Cavity Surface-Emitting Lasers by a Coupled Nonequilibrium Green's Function-Drift-Diffusion Approach, *Phys. Rev. Appl.* **14**, 024037 (2020).
- [13] R. C. Bowen, G. Klimeck, R. K. Lake, W. R. Frensley, and T. Moise, Quantitative simulation of a resonant tunneling diode, *J. Appl. Phys.* **81**, 3207 (1997).
- [14] J. Wang, E. Polizzi, and M. Lundstrom, A three-dimensional quantum simulation of silicon nanowire transistors with the effective-mass approximation, *J. Appl. Phys.* **96**, 2192 (2004).
- [15] M. Luisier and G. Klimeck, Simulation of nanowire tunneling transistors: From the Wentzel-Kramers-Brillouin approximation to full-band phonon-assisted tunneling, *J. Appl. Phys.* **107**, 084507 (2010).
- [16] M. Pourfath and H. Kosina, Computational study of carbon-based electronics, *J. Comput. Electron.* **8**, 427 (2009).
- [17] A. Shedbalkar, Z. Andreev, and B. Witzigmann, Simulation of an indium gallium nitride quantum well light-emitting diode with the non-equilibrium Green's function method, *Phys. Status Solidi (b)* **253**, 158 (2015).
- [18] S. Steiger, R. G. Veprek, and B. Witzigmann, in *2009 13th Int. Workshop Comput. Electron.* (2009), p. 1.
- [19] R. Wang, Y. Zhang, F. Bi, T. Frauenheim, G. Chen, and C. Yam, Quantum mechanical modeling the emission pattern and polarization of nanoscale light emitting diodes, *Nanoscale* **8**, 13168 (2016).
- [20] L. E. Henrickson, Nonequilibrium photocurrent modeling in resonant tunneling photodetectors, *J. Appl. Phys.* **91**, 6273 (2002).
- [21] N. Dehdashti Akhavan, G. A. Umana-Membreno, R. Gu, M. Asadnia, J. Antoszewski, and L. Faraone, Superlattice barrier HgCdTe nBn infrared photodetectors: Validation of the effective mass approximation, *IEEE Trans. Electron Devices* **63**, 4811 (2016).
- [22] M. A. Naser, M. J. Deen, and D. A. Thompson, Photocurrent modeling and detectivity optimization in a resonant-tunneling quantum-dot infrared photodetector, *IEEE J. Quantum Electron.* **46**, 849 (2010).
- [23] U. Aeberhard and R. Morf, Microscopic nonequilibrium theory of quantum well solar cells, *Phys. Rev. B* **77**, 125343 (2008).
- [24] U. Aeberhard, Simulation of ultrathin solar cells: Beyond the limits of the semiclassical bulk picture, *IEEE J. Photovolt.* **6**, 654 (2016).
- [25] N. Cavassilas, F. Michelini, and M. Bescond, Modeling of nanoscale solar cells: The Green's function formalism, *J. Renew. Sustain. Energy* **6**, 011203 (2014).
- [26] T. Kubis, C. Yeh, P. Vogl, A. Benz, G. Fasching, and C. Deutsch, Theory of nonequilibrium quantum transport and energy dissipation in terahertz quantum cascade lasers, *Phys. Rev. B* **79**, 195323 (2009).
- [27] S.-C. Lee and A. Wacker, Nonequilibrium Green's function theory for transport and gain properties of quantum cascade structures, *Phys. Rev. B* **66**, 245314 (2002).
- [28] G. Hałdaś, A. Kolek, and I. Tralle, Modeling of mid-infrared quantum cascade laser by means of nonequilibrium Green's functions, *IEEE J. Quantum Electron.* **47**, 878 (2011).
- [29] T. Grange, Contrasting influence of charged impurities on transport and gain in terahertz quantum cascade lasers, *Phys. Rev. B* **92**, 241306 (2015).
- [30] J. M. Miloszewski and M. S. Wartak, Semiconductor laser simulations using non-equilibrium Green's functions, *J. Appl. Phys.* **111**, 053104 (2012).
- [31] T. Grange, Electron transport in quantum wire superlattices, *Phys. Rev. B* **89**, 165310 (2014).
- [32] F. Bertazzi, A. Tibaldi, M. Goano, J. A. G. Montoya, and E. Bellotti, Nonequilibrium Green's Function Modeling of Type-II Superlattice Detectors and its Connection to Semiclassical Approaches, *Phys. Rev. Appl.* **14**, 014083 (2020).
- [33] E. Bellotti, F. Bertazzi, A. Tibaldi, J. Schuster, J. Bajaj, and M. Reed, Disorder-Induced Degradation of Vertical Carrier Transport in Strain-Balanced Antimony-Based Superlattices, *Phys. Rev. Appl.* **16**, 054028 (2021).
- [34] U. Aeberhard, A. Gonzalo, and J. M. Ulloa, Photocarrier extraction in GaAsSb/GaAsN type-II QW superlattice solar cells, *Appl. Phys. Lett.* **112**, 213904 (2018).
- [35] I. Vurgaftman, J. R. Meyer, and L. R. Ram-Mohan, Band parameters for III-V compound semiconductors and their alloys, *J. Appl. Phys.* **89**, 5815 (2001).
- [36] J. Z. Huang, W. C. Chew, J. Peng, C.-Y. Yam, L. J. Jiang, and G.-H. Chen, Model order reduction for multiband quantum transport simulations and its application to p-type junctionless transistors, *IEEE Trans. Electron Devices* **60**, 2111 (2013).
- [37] H. Carrillo-Nuñez, A. Ziegler, M. Luisier, and A. Schenk, Modeling direct band-to-band tunneling: From bulk to quantum-confined semiconductor devices, *J. Appl. Phys.* **117**, 234501 (2015).
- [38] H. Carrillo-Nuñez, J. Lee, S. Berrada, C. Medina-Bailon, M. Luisier, A. Asenov, and V. Georgiev, Efficient two-band based non-equilibrium Green's function scheme for modeling tunneling nano-devices, 2015 Int. Conf. Simulation Semicond. Processes Devices (SISPAD), 141 (2018).
- [39] A. Pan and C. O. Chui, Modeling direct interband tunneling. II. Lower-dimensional structures, *J. Appl. Phys.* **116**, 054509 (2014).
- [40] C. Alper, M. Visciarelli, P. Palestri, J. Padilla, A. Gnani, E. Gnani, and A. Ionescu, Modeling the imaginary branch in III-V tunneling devices: Effective mass vs $k \cdot p$, 2015 Int. Conf. Simulation Semicond. Processes Devices (SISPAD), 273 (2015).
- [41] S. Jin, A.-T. Pham, W. Choi, M. A. Pourghaderi, J. Kim, and K.-H. Lee, Performance evaluation of FinFETs: From multisubband BTE to DD calibration, 2016 Int. Conf.

- Simulation Semicond. Processes Devices (SISPAD), 109 (2016).
- [42] C. Sirtori, F. Capasso, J. Faist, and S. Scandolo, Non-parabolicity and a sum rule associated with bound-to-bound and bound-to-continuum intersubband transitions in quantum wells, *Phys. Rev. B* **50**, 8663 (1994).
- [43] P. Würfel and U. Würfel, *Physics of Solar Cells: From Basic Principles to Advanced Concepts* (Wiley, Weinheim, Germany, 2016).
- [44] S. Datta, *Electronic Transport in Mesoscopic Systems, Cambridge Studies in Semiconductor Physics and Microelectronic Engineering* (Cambridge University Press, Cambridge, UK, 1982).
- [45] R. Lake, G. Klimeck, R. C. Bowen, and D. Jovanovic, Single and multiband modeling of quantum electron transport through layered semiconductor devices, *J. Appl. Phys.* **81**, 7845 (1997).
- [46] A. Svizhenko, M. P. Anantram, T. R. Govindan, B. Biegel, and R. Venugopal, Two-dimensional quantum mechanical modeling of nanotransistors, *J. Appl. Phys.* **91**, 2343 (2002).
- [47] U. Aeberhard, Quantum-kinetic theory of photocurrent generation via direct and phonon-mediated optical transitions, *Phys. Rev. B* **84**, 035454 (2011).
- [48] G. Hałdaś, Implementation of non-uniform mesh in non-equilibrium Green's function simulations of quantum cascade lasers, *J. Comput. Electron.* **18**, 1400 (2019).
- [49] A. Pan and C. O. Chui, Modeling direct interband tunneling. I. Bulk semiconductors, *J. Appl. Phys.* **116**, 054508 (2014).
- [50] H. Ilatikhameneh, R. B. Salazar, G. Klimeck, R. Rahman, and J. Appenzeller, From Fowler-Nordheim to nonequilibrium Green's function modeling of tunneling, *IEEE Trans. Electron Devices* **63**, 2871 (2016).
- [51] L. Bürkle, F. Fuchs, E. Ahlswede, W. Pletschen, and J. Schmitz, Wannier-Stark localization in InAs/(GaIn)Sb superlattice diodes, *Phys. Rev. B* **64**, 045315 (2001).
- [52] C. Hamaguchi, M. Yamaguchi, H. Nagasawa, M. Morifuji, A. D. Carlo, P. Vogl, G. Böhm, G. Tränkle, G. Weimann, Y. Nishikawa, and S. Muto, Wannier-Stark localization in superlattices, *Jpn. J. Appl. Phys.* **34**, 4519 (1995).
- [53] B.-M. Nguyen, D. Hoffman, P.-Y. Delaunay, and M. Razeghi, Dark current suppression in type-II InAs/GaSb superlattice long wavelength infrared photodiodes with M-structure barrier, *Appl. Phys. Lett.* **91**, 163511 (2007).
- [54] Y. Wei, A. Hood, H. Yau, A. Gin, M. Razeghi, M. Tidrow, and V. Nathan, Uncooled operation of type-II InAs/GaSb superlattice photodiodes in the midwavelength infrared range, *Appl. Phys. Lett.* **86**, 233106 (2005).
- [55] A. Kazemi, S. Myers, Z. Taghipour, S. Mathews, T. Schuler-Sandy, S. Lee, V. M. Cowan, E. Garduno, E. Steenbergen, C. Morath, G. Ariyawansa, J. Scheihing, and S. Krishna, Mid-wavelength infrared unipolar nBp superlattice photodetector, *Infrared Phys. Technol.* **88**, 114 (2018).
- [56] M. Delmas, J.-B. Rodriguez, R. Rossignol, A. S. Licht, E. Giard, I. Ribet-Mohamed, and P. Christol, Identification of a limiting mechanism in GaSb-rich superlattice midwave infrared detector, *J. Appl. Phys.* **119**, 174503 (2016).
- [57] A. A. Ignatov, E. P. Dodin, and V. I. Shashkin, Transient response theory of semiconductor superlattices: Connection with Bloch oscillations, *Mod. Phys. Lett. B* **5**, 1087 (1991).
- [58] S. Rott, P. Binder, N. Linder, and G. H. Döhler, A combined model for miniband and hopping transport in superlattices, *Phys. E Low-Dimens. Systems Nanostruct.* **2**, 511 (1998).
- [59] S. Feng, C. H. Grein, and M. E. Flatté, Effects of impurity scattering on electron-phonon resonances in semiconductor superlattice high-field transport, *Phys. Rev. B* **68**, 085307 (2003).
- [60] P. Kleinert and V. V. Bryksin, Zener antiresonance in the quantum diffusion of semiconductor superlattices, *J. Phys.: Condens. Matter* **16**, 4441 (2004).
- [61] D. Esseni, M. Pala, P. Palestri, C. Alper, and T. Rollo, A review of selected topics in physics based modeling for tunnel field-effect transistors, *Semicond. Sci. Technol.* **32**, 083005 (2017).
- [62] A. Kolek, Nonequilibrium Green's function formulation of intersubband absorption for nonparabolic single-band effective mass Hamiltonian, *Appl. Phys. Lett.* **106**, 181102 (2015).
- [63] J. Piprek, Efficiency droop in nitride-based light-emitting diodes, *Phys. Status Solidi (a)* **207**, 2217 (2010).
- [64] M. Auf der Maur, Multiscale approaches for the simulation of optoelectronic devices, *J. Green Eng.* **5**, 133 (2016).